Published by Avanti Publishers

International Journal of Petroleum Technology

ISSN (online): 2409-787X

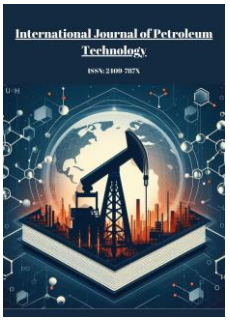

Pore-scale Competitive Migration and Selective Regulation of Multi-component Hydrocarbons in Continental Shale Oil: A Phase-field Modeling Study

Fuqiang Xu[1,2], Zhigang Liu[1], Can Ji[1,*], Rubing Han[1], Yan Liu[1] and Aimin Chen[1]

[1]*Energy Research Institute, Qilu University of Technology (Shandong Academy of Sciences), Jinan 250014, Shandong, China*

[2]*Engineering Research Center of Geothermal Resources Development Technology and Equipment, Ministry of Education, Jilin University, Changchun 130026, Jilin, China*

ARTICLE INFO

Article Type: Research Article

Academic Editor: Joshua Gorimbo

Keywords:
Phase-field model
Continental shale oil
Competitive seepage
Pore-scale simulation
Multi-component hydrocarbon migration

Timeline:
Received: May 06, 2026
Accepted: June 10, 2026
Published: June 15, 2026

Citation: Xu F, Liu Z, Ji C, Han R, Liu Y, Chen A. Pore-scale competitive migration and selective regulation of multi-component hydrocarbons in continental shale oil: A phase-field modeling study. Int J Pet Technol. 2026; 13(1): 29-42.

DOI: https: //doi.org/10.15377/2409-787X.2026.13.3

ABSTRACT

Continental shale oil is a vital alternative resource for oil and gas reserve and production growth in China. However, strong reservoir heterogeneity, widely developed micro-nano pore throats and complex multi-component crude oil properties lead to low crude oil producing degree and restrict efficient large-scale development. Most existing seepage studies are based on single-component assumptions, failing to fully reveal multi-component differential migration, competitive seepage mechanisms and the threshold regulation effect of pore scale. To address this issue, this study builds a pore-scale multi-component seepage model through numerical simulation, divides hydrocarbons into light, medium and heavy components, and systematically analyzes migration characteristics under varying injection flow rates and particle radii. The results show that component properties dominate differential migration and competitive seepage: light components with strong convection and diffusion capacities preferentially occupy dominant seepage channels and gradually compress the flow space of medium and heavy components. Within the range of 1.0-3.0 g/s, injection flow rate has a weak influence on the multi-component distribution pattern and does not alter the relative migration capacity of each component. Pore scale imposes selective regulation with a distinct threshold effect: heavier components are more sensitive to pore tightening, and the inter-component migration capacity gap widens sharply when the throat width shrinks below a critical value of $\delta_{cr} \in (5, 10)$ mm (corresponding to a critical particle radius $r_{cr} \in (20.0, 22.5)$ mm and a constriction ratio $\alpha_{cr} \in (0.10, 0.20)$). This study deepens the understanding of multi-component microscopic migration mechanisms of continental shale oil, and provides theoretical support for reservoir producing degree evaluation, development parameter optimization and hierarchical reservoir stimulation.

*Corresponding Author

Email: jic@sderi.cn

1. Introduction

Continental shale oil serves as a vital alternative resource for increasing oil and gas reserves and production in China [1], and it has considerable resource scale and development potential, and is of great significance for ensuring national energy security. Continental shale in China features diverse sedimentary environments and strong reservoir heterogeneity [2]. Multiple pore types including organic matter pores, intergranular pores and intragranular pores are developed, with most pore-throat sizes in the micro-nano scale. Affected jointly by the complex pore structure and inherent properties of hydrocarbons, the microscopic migration process of shale oil in reservoirs is highly complicated [3, 4]. Low producing degree of crude oil and rapid production decline of single wells are prominent challenges in current development. Clarifying the migration laws and mechanisms of hydrocarbon fluids at the pore scale is the key scientific foundation for efficient development of continental shale oil [5-7].

Considerable progress has been made in shale oil seepage research. Previous works have revealed typical micro-nano scale seepage features including boundary layer effect, adsorption-retention, slippage and nonlinear flow, and clarified the influences of pore scale, fluid properties and displacement conditions, laying a fundamental basis for understanding shale oil migration mechanisms [8-10]. For pore-scale numerical simulation, the phase-field method has become a mainstream tool for multiphase flow modeling owing to its capability to track fluid interfaces spontaneously [11, 12]. Existing phase-field studies have been extensively conducted for single-component fluid flow and two-phase oil-water displacement in porous media, and have systematically uncovered the impacts of wettability, capillary force and pore geometry on displacement dynamics [13, 14]. Nevertheless, most phase-field simulations are still limited to single-component or simple two-component systems. Few efforts have been devoted to the competitive migration of light, medium and heavy hydrocarbon fractions in continental shale oil, and quantitative investigations on differential migration mechanisms and threshold regulation effects among multi-component hydrocarbons remain scarce [5, 15]. Overall, most existing studies adopt the whole hydrocarbon system or single-component assumption, neglecting internal component differences and their differentiated impacts on migration processes.

In fact, shale oil is a complex mixture of light, medium, heavy hydrocarbons and asphaltenes, with significant discrepancies in molecular size, viscosity, diffusion coefficient and adsorption property across components [16, 17]. In micro-nano pore reservoirs, such property differences are further amplified by pore structures, resulting in distinct migration capacity, occurrence state and swept range, as well as competitive seepage and space occupation among components [18, 19]. At present, quantitative investigations on the spatiotemporal evolution of multi-component differential migration and inter-component interaction mechanisms are still inadequate. In addition, injection parameters and pore structure are two critical factors regulating hydrocarbon migration [5, 20]. Existing studies mainly focus on the impacts of injection flow rate on overall seepage rate and displacement efficiency, while the differential responses of multi-component hydrocarbons under varying flow rates remain poorly understood [21]. For pore structure, although pore-throat size directly governs fluid flowability and wall adsorption intensity, the evolution of multi-component migration capacity during pore densification lacks in-depth insight [22, 23]. In particular, whether a differentiation threshold effect exists when pore-throat size shrinks to a critical range still needs further clarification [24]. China's continental shale reservoirs feature complex pore structures, strong heterogeneity and large fluctuations in crude oil components [2, 25]. The single-component-based seepage theory can neither accurately evaluate the producing potential of different hydrocarbon components, nor provide sufficient theoretical support for development parameter optimization and hierarchical reservoir stimulation [26, 27]. Therefore, research on multi-component differential migration laws and regulation mechanisms at the pore scale is essential for improving shale oil microscopic seepage theory and precise reservoir producing degree evaluation.

To address the above research gaps, this paper takes the microscopic migration process of continental shale oil as the research object and establishes a pore-scale multi-component seepage model based on the phase-field method. The core scientific contributions of this work are summarized as follows: (1) A phase-field simulation framework for multi-component hydrocarbons (light, medium and heavy fractions) in continental shale oil is constructed, which enables the characterization of competitive seepage and spatial occupation among different

hydrocarbon components in porous media; (2) The mechanism of competitive migration and selective regulation of multi-component hydrocarbons at the pore scale is revealed, and the differential response laws of each component to injection flow rate and pore structure parameters are clarified; (3) The threshold effect of pore-scale hydrocarbon migration is quantitatively identified, and the critical criterion of pore-throat size for differential migration of multi-component hydrocarbons is defined. This study can deepen the understanding of multi-component migration mechanisms of continental shale oil at the pore scale and enrich the theoretical system of microscopic seepage. Meanwhile, it provides a theoretical basis for reservoir producing degree evaluation, development parameter optimization.

2. Mathematical Descriptions

To focus on the competitive migration dynamics of multi-component hydrocarbons in pore spaces over a short time scale, the present model is built upon the following simplified assumptions, the rationality of which under the target research scenario is supported by relevant published studies: (1) The fluid and rock matrix satisfy the local thermal equilibrium condition [28, 29]. This assumption is widely accepted in pore-scale isothermal seepage studies of shale reservoirs, as temperature fluctuation during short-term displacement is negligible and imposes no significant influence on flow behaviors. (2) No chemical reaction occurs between the fluid and the rock matrix [30, 31]. For short-duration pore-scale migration processes under in-situ reservoir temperature, geochemical effects such as mineral dissolution, precipitation and hydrocarbon cracking are extremely weak and can be reasonably excluded from the flow simulation. (3) Rock matrix deformation is not considered in this study, and relevant investigations will be conducted in future work [32, 33]. Owing to the high mechanical strength and ultra-low permeability of continental shale formations, pore structure deformation caused by short-term fluid flow is very limited. The rigid porous medium assumption has been extensively adopted in similar pore-scale numerical simulations of shale oil seepage. (4) Hydrocarbons are classified into three fractions by molecular mass: light, medium and heavy fractions. Inter-component mass transfer and partial miscibility are neglected in this work. The mutual solubility among these fractions is poor, and only negligible inter-fraction mixing occurs during the short migration process, which justifies the immiscible phase assumption. The three fractions are denoted as phase A, phase B and phase C respectively, and their key physical parameters are summarized in Table **1** [34, 35].

Notably, the above simplifications also define the applicable boundary of the current model. In actual continental shale reservoirs, long-term production and changing pressure-temperature conditions may induce partial miscibility among hydrocarbon fractions, component partitioning, weak geochemical reactions and rock skeleton deformation, which would modify the competitive seepage patterns and interface evolution to a certain degree. These complex physical and chemical effects will be systematically incorporated in our subsequent work to improve the model's adaptability to real reservoir conditions.

Table 1: The parameters of the hydrocarbon components [34, 35].

Component	Heat Capacity, J/(kg·℃)	Dynamic Viscosity, mPa·s	Density, kg/m³	Thermal Conductivity, W/(m·℃)
Light (*A*), C_5-C_{10}	3000	0.0126	170	0.03
Medium (*B*), C_{11}-C_{20}	2200	5	800	0.15
Heavy (*C*), C_{21+}	2000	50	950	0.14

For three-phase immiscible systems, the phase-field model is established based on the free energy formulation of the target system. Three independent phase-field variables are defined, with each corresponding to one single phase [36]. The Cahn–Hilliard equations act as the core governing equations of the model, and their specific expressions are given as follows [37, 38]:

$$\begin{cases} \frac{\partial \psi_i}{\partial t} + \nabla \cdot (\psi_i \vec{u}) = \nabla \cdot \frac{M_0}{\Sigma_i} \nabla \eta_i, \quad i = A, B, C \\ \psi_A + \psi_B + \psi_C = 1 \\ \eta_i = \frac{12\Sigma_A\Sigma_B\Sigma_C}{\varepsilon(\Sigma_B\Sigma_C + \Sigma_A\Sigma_C + \Sigma_A\Sigma_B)} \sum_{j \neq i} \left(\frac{1}{\Sigma_j} \left(\partial_i F(\boldsymbol{\psi}) - \partial_j F(\boldsymbol{\psi}) \right) \right) - \frac{3}{4} \varepsilon \Sigma_i \nabla^2 \psi_i \end{cases} \tag{1}$$

where ψ_i is the phase-field variable, with subscripts *i* representing phase *A*, phase *B*, and phase *C*, respectively; *t* (s) is the time; $\vec{u}$ (m/s) is the fluid velocity; M_0 (m^3/s) is the mobility tuning parameter; Σ_i (Pa) is the capillary terms; η_i (Pa) is the generalized chemical potentials; $F(\boldsymbol{\psi})$ (Pa) is the Bulk energy; ε is the parameter controlling interface thickness.

The expressions for $F(\boldsymbol{\psi})$, $\sum_A$, $\sum_B$, and $\sum_C$ are as follows [39]:

$$\begin{cases} \Sigma_i = \sigma_{i,j} + \sigma_{i,k} - \sigma_{j,k} \\ \Sigma_A = \sigma_{AB} + \sigma_{AC} - \sigma_{BC} \\ \Sigma_B = \sigma_{AB} + \sigma_{BC} - \sigma_{AC} \\ \Sigma_C = \sigma_{BC} + \sigma_{AC} - \sigma_{AB} \end{cases} \tag{2}$$

$$F(\boldsymbol{\psi}) = \sigma_{AB}{\psi_A}^2{\psi_B}^2 + \sigma_{AC}{\psi_A}^2{\psi_C}^2 + \sigma_{BC}{\psi_B}^2{\psi_C}^2 + \Lambda{\psi_A}^2{\psi_B}^2{\psi_C}^2 \quad + \psi_A\psi_B\psi_C(\Sigma_A\psi_A + \Sigma_B\psi_B + \Sigma_C\psi_C) \tag{3}$$

where σ is the surface tensions; σ_{AB}, σ_{AC} and σ_{BC} respectively represent the surface tensions between phases *A*-*B*, *A*-*C*, and *B*-*C*; ∧ (Pa) is the additional free Bulk energy.

The fluid flow process follows the conservation laws of mass and momentum. The continuity equation and Navier–Stokes equations are adopted for numerical computation to describe the two conservation laws respectively [40, 41]:

$$\begin{cases} \rho_f \frac{\partial \vec{u}}{\partial t} + \rho_f(\vec{u}\cdot\nabla)\vec{u} = \nabla\cdot[-\rho_f 2\mathbf{I} + \mathbf{K}] + \mathbf{F} + \mathbf{F}_{st} \\ \rho_f \nabla\cdot\vec{u} = 0 \\ \mathbf{K} = \mu_f(\nabla\vec{u} + (\nabla\vec{u})^T) \\ \mathbf{F}_{s_t} = \sum_{i=A,B,C}(\eta_i\nabla\psi_i) \end{cases} \tag{4}$$

$$\begin{cases} \rho_f = \psi_A\rho_A + \psi_B\rho_B + \psi_C\rho_C \\ \mu_f = \psi_A\mu_A + \psi_B\mu_B + \psi_C\mu_C \end{cases} \tag{5}$$

where ρ_f (kg/m^3) is the fluid density; **I** is the identity matrix; **F** (N/m^3) is the volume force vector; $\mathbf{F}_{st}$ (N/m^3) is the surface tension force; **K** (Pa) is the viscous stress tensor; μ_f (Pa·s) is the fluid viscosity.

Heat transfer is characterized by an independent governing equation. The effective thermal conductivity and heat capacity of the fluid are calculated via the weighted averaging method [42]:

$$\begin{cases} \left(\rho c_p\right)_{eff}\frac{\partial T}{\partial t} + \rho_f c_{p,f}\nabla\cdot(\vec{u}\cdot T) - \nabla\cdot\left(\lambda_{eff}\nabla T\right) = Q \\ \left(\rho c_p\right)_{eff} = (1-\varphi)\rho_s c_{p,s} + \varphi\rho_f c_{p,f} \\ \lambda_{eff} = (1-\varphi)\lambda_s + \varphi\lambda_f \end{cases} \tag{6}$$

$$\begin{cases} c_f = \frac{\psi_A\rho_A c_A + \psi_B\rho_B c_B + \psi_C\rho_C c_C}{\psi_A\rho_A + \psi_B\rho_B + \psi_C\rho_C} \\ \lambda_f = \frac{\psi_A\rho_A\lambda_A + \psi_B\rho_B\lambda_B + \psi_C\rho_C\lambda_C}{\psi_A\lambda_A + \psi_B\lambda_B + \psi_C\lambda_C} \end{cases} \tag{7}$$

where $(\rho c_p)_{eff}$ (J/(m^3·℃)) and λ_{eff} (W/(m·℃)) are the effective volumetric capacity and thermal conductivity, respectively; ρ_s (kg/m^3) is solid density; $c_{p,s}$ (J/(kg·℃)) and $c_{p,f}$ (J/(kg·℃)) are the solid and fluid thermal capacity, respectively; λ_s (W/(m·℃)) and λ_f (W/(m·℃)) are the solid and fluid thermal conductivity, respectively; *Q* (W/m^3) is the energy source term; φ is the porosity; *T* (℃) is the temperature.

The scientific validity and computational reliability of this phase-field model have been systematically verified by Boyer et al. using classical analytical solutions and laboratory experimental data [39]. For typical cases including three-phase lens spreading and bubble penetration across stratified fluids, their numerical outputs show good agreement with Young's equation and the Laplace law of pressure discontinuity, with the relative error of pressure calculation falling in the range of 0.45% to 1.03%. In this study, only the reservoir parameters of the Qingshankou Formation are substituted into the model [39, 42], while the fundamental mathematical framework of the original

model remains unmodified. Accordingly, the numerical stability and physical rationality of the model adopted in this work are fully consistent with the verified conclusions reported in the reference.

3. Geometric Descriptions

The numerical model is established within a rectangular domain measuring 0.8 m in length and 0.4 m in height, which consists of matrix particles and pore throats (Fig. **1a**). All fluid storage and transport processes occur exclusively within the pore throat space. Although the model is geometrically scaled up to tackle the computational challenges and interface capture difficulties of micro-nano-scale simulations, it adopts flow similarity criteria to ensure core dimensionless numbers match those of real shale reservoirs, so that it can faithfully reproduce core physical processes such as multi-component immiscible migration, interface evolution and thermo-hydro coupling. The pore-throat width δ is defined as the minimum gap between two adjacent matrix particles, which is determined geometrically by $\delta = L\text{-}2r$, where L = 50 mm is the fixed center-to-center spacing and r is the particle radius (In the baseline scenario, matrix particles are set to a diameter of 30 mm). To investigate the effect of pore-scale tightening on multi-component migration, five particle radii are considered: r = 12.5, 15.0, 17.5, 20.0 and 22.5 mm, corresponding to throat widths of δ = 25, 20, 15, 10 and 5 mm, respectively. The dimensionless throat constriction ratio $\alpha = \delta/L$ is further introduced to characterize the relative degree of pore constriction, with α ranging from 0.50 to 0.10 across the simulated cases.

The model is discretized using unstructured triangular meshes (Fig. **1b**), with a total of 190,900 degrees of freedom (DOF), which strikes an optimal balance between numerical accuracy and computational efficiency, as shown in Table **2**.

Table 2: Grid independence analysis.

Degrees of Freedom	Volume Fractions of Light Components	Calculation Time, Min
318000	0.480	244
243000	0.481	147
190900	0.482	91
143800	0.483	69
72500	0.492	53

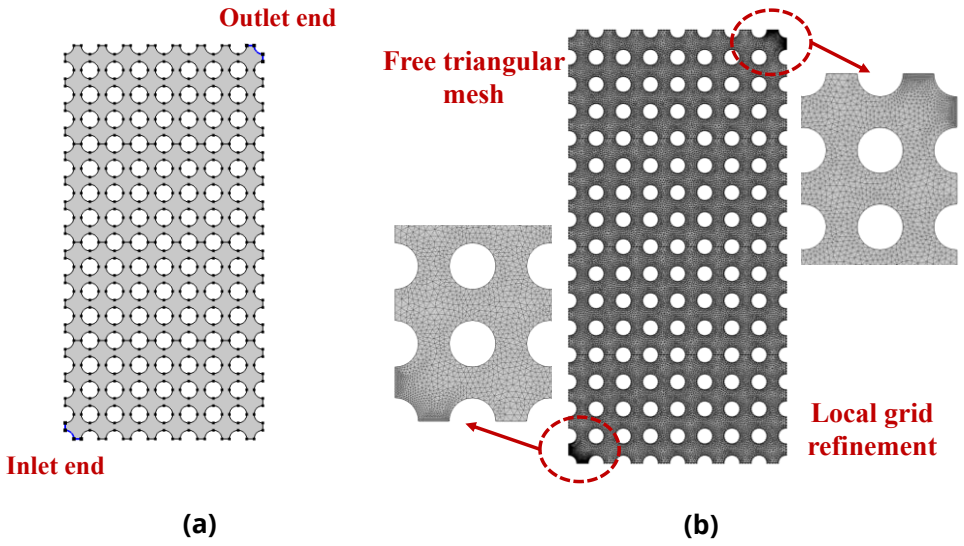

Figure 1: Calculation domain and mesh discretization scheme of the model: **(a)** calculation domain; **(b)** mesh.

An injection section is placed at the bottom-left corner of the domain under a constant flow rate of 2 g/s, while a production section is set at the top-right corner with its pressure maintained at the initial level. All remaining boundaries are specified as no-flow and adiabatic boundaries to replicate the geological environment of in-source shale oil migration. The top of the computational domain is assigned a temperature of 90 ℃ and a pressure of 30 MPa, corresponding to a pressure gradient of 10,000 Pa/m and a temperature gradient of 0.035 ℃/m. This configuration mimics the instantaneous overpressure field and temperature difference triggered by hydrocarbon generation expansion during source rock maturation, which acts as the initial driving force for multi-component hydrocarbon migration.

Three hydrocarbon fractions (heavy, medium and light) are initially distributed in the pores of the porous medium to reproduce the multiphase transport process, with initial volume fractions of 0.25, 0.45 and 0.30 respectively. The interfacial tension coefficients for heavy-medium, heavy-light and medium-light phase pairs are set to 10 mN/m, 15 mN/m and 12 mN/m, respectively. Values of other physical parameters are summarized in Table **3**, all determined through comprehensive analysis of shale oil reservoir properties in the Songliao Basin [35, 42]. Although the model is reasonably upscaled in apparent geometric scale, the core physical processes it captures, such as multi-component immiscible migration, interface evolution and thermal-hydraulic coupling, are largely consistent with those in real shale reservoirs, and all quantitative parameters have solid geological foundations.

The total simulation lasts for 6 s with a fixed time step of 0.05 s, and a relative tolerance of 0.001 is defined as the convergence criterion. The model construction and meshing are completed via the finite element software COMSOL Multiphysics, and numerical calculations are carried out in combination with MATLAB.

Table 3: The parameters of the reservoir properties [35, 42].

Component	Value
Heat capacity, J/(kg·℃)	900
Porosity, %	65
Density, kg/m^3	2550
Thermal conductivity, W/(m·℃)	2.6

4. Results Analysis

4.1. Migration Characteristics

Fig. (**2**) presents the spatiotemporal distribution evolution of light, medium, and heavy hydrocarbon components during migration in porous media, reflecting the control mechanism of component property differences on microscopic migration behaviors. The light component (Fig. **2a**) has the widest swept range and the farthest displacement front within the same migration time, and its concentration field shows an overall continuous banded distribution. The light component features small molecular size and low viscosity. It has strong capacities for convective transport and molecular diffusion, and is weakly affected by adsorption retardation on pore walls and throat snapping effects. Thus, it can pass through pore throats smoothly and migrate toward the upper part of the model. The high volume fraction of light components in the upper region arises from the limited outlet size, which hinders fluid discharge and causes fluid accumulation near the production section.

For the medium component (Fig. **2b**), both the swept range and front propagation rate are lower than those of the light component. Its displacement front has an irregular shape, with obvious flow bypassing and local retention in throat regions. This occurs because the molecular diffusion of medium-molecular-weight hydrocarbons is significantly weakened, and convection dominates the migration process. The microscopic restriction effect of the pore structure gradually becomes prominent, and the throttling effect of throats begins to noticeably hinder component migration. The heavy component (Fig. **2c**) has the most limited distribution range. It

largely accumulates in the space near the injection end, and its displacement front advances slowly with a clustered distribution. The underlying reasons are the large molecular weight and high viscosity of heavy components. On one hand, viscous resistance during seepage increases significantly, and heavy components are prone to adsorption and retention on pore walls. On the other hand, heavy component fluids easily break when passing through throats and induce the Jamin effect. As a result, its overall migration efficiency is much lower than that of light and medium components.

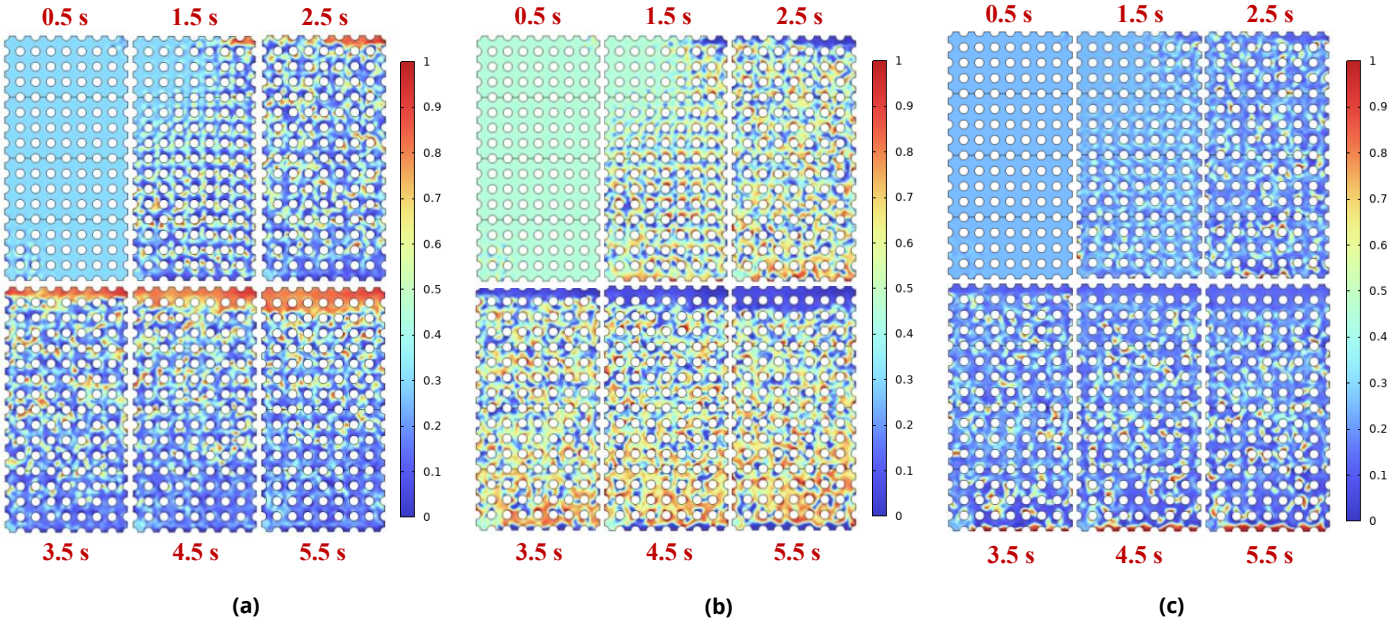

Figure 2: Spatiotemporal distribution characteristics of different hydrocarbon components: **(a)** light components; **(b)** medium components; **(c)** heavy components.

Fig. (**3**) quantitatively describes the evolution of the distribution area of the three hydrocarbon components over time. Overall, the distribution area of light components shows a continuous linear growth trend with migration time, while those of medium and heavy components both decrease slowly. The distribution area of light components expands steadily over time, with a positive fitting slope and stable growth rate. This indicates that light components maintain strong migration capacity throughout the migration cycle, which is consistent with the microscopic distribution characteristics in Fig. (**2**).

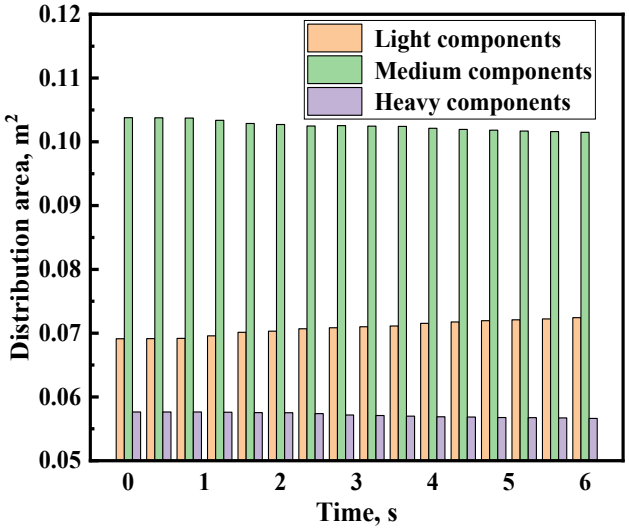

Figure 3: Temporal evolution of distribution areas for different hydrocarbon components.

$$\begin{cases} S_A = 0.0006t + 0.0690 \\ S_B = -0.0004t + 0.1037 \\ S_C = -0.0002t + 0.0578 \end{cases} \quad (8)$$

where, S_A, S_B and S_C are the distribution areas of light components, medium components, and heavy components, respectively, m^2.

The distribution areas of medium and heavy components both decrease slightly over time, with fitting slopes of −0.0004 and −0.0002 respectively, as shown in Eq. (**8**). The medium component has a relatively more significant decline due to its largest initial distribution area and larger base value. This phenomenon results from the combined effects of multi-component competitive seepage and property limitations. On one hand, light components migrate faster, preferentially occupy dominant seepage channels, and gradually occupy the flow space of medium and heavy components, leading to continuous compression of their effective distribution ranges. On the other hand, medium and heavy components have high migration resistance. They are prone to adsorption and retention on pore walls, as well as throat snapping and the Jamin effect in throats, which make it difficult to expand into upper pores. Therefore, their overall distribution ranges gradually shrink during migration.

4.2. Parameter Effects

Fig. (**4**) and Fig. (**5**) together present the quantitative comparison of spatial distribution characteristics and distribution area proportions of the three hydrocarbon components under different injection flow rates at a migration time of 1.5 s. Overall, within the injection flow rate range of 1.0 – 3.0 g/s, flow rate variation has weak effects on the distribution pattern and relative proportions of hydrocarbon components, and the differential migration law of the three components remains basically stable.

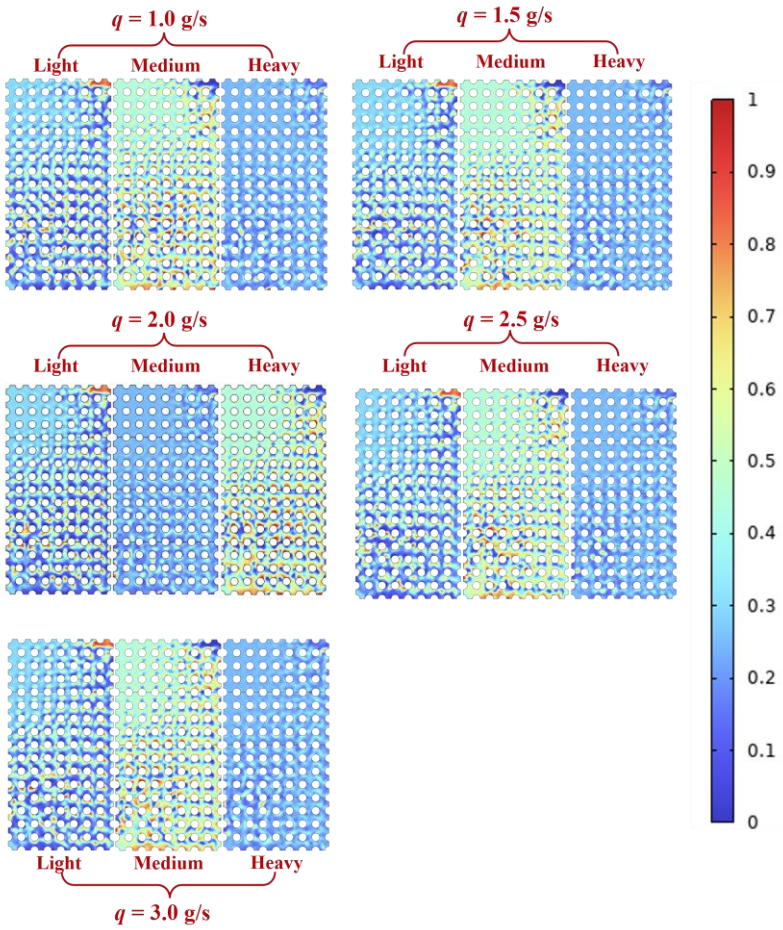

Figure 4: Comparison of distribution characteristics of different hydrocarbon components under various flow rates (1.5 s).

The quantitative statistical results are shown in Fig. (**5**). As the injection flow rate increases gradually from 1.0 g/s to 3.0 g/s, the distribution area proportions of light, medium, and heavy components show no significant fluctuations. The proportion of light components remains at approximately 30%, that of medium components stabilizes in the range of 44% – 45%, and that of heavy components stays around 25%. The ranking and relative differences of the proportions of the three components remain unchanged. The average proportions over the entire flow rate range (Fig. **5b**) are 30.32% for light components, 44.71% for medium components, and 24.97% for heavy components, with minimal deviation from the statistical results under a single flow rate. This further confirms that flow rate variation does not exert a substantial impact on the overall proportional relationship of component distribution.

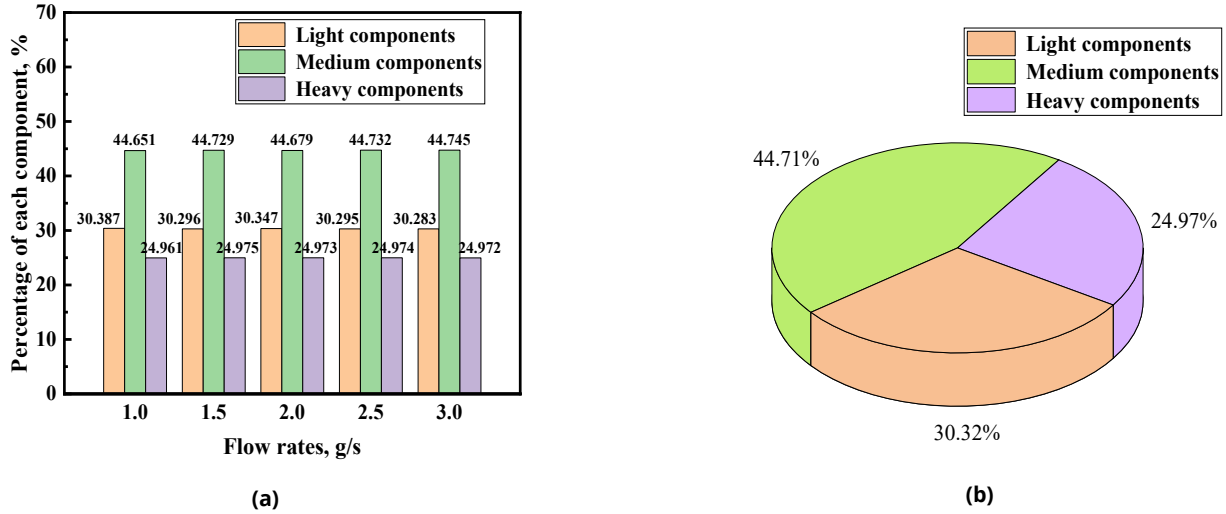

Figure 5: Comparison of distribution area proportions of different hydrocarbon components under various flow rates (1.5 s): **(a)** overall characteristics; **(b)** average values.

In terms of spatial distribution morphology (Fig. **4**), the displacement front positions, swept ranges, and accumulation characteristics of the three components are highly similar under different injection flow rates. Light components show a relatively wider sweeping capacity, medium components occupy the main distribution area, and heavy components are relatively concentrated near the injection end. No abrupt change in distribution pattern or reversal of migration law occurs with increasing flow rate. The underlying reason is that within the flow rate range set in this study, the core controlling factors of hydrocarbon component migration are still the intrinsic property differences of components (molecular size, viscosity, diffusion coefficient) and the structural restriction of porous media. The increase in injection flow rate only enhances the displacement driving force as a whole, but does not change the relative strength of migration capacity among the three components. Therefore, the differential migration pattern and distribution proportions among components remain basically stable.

Fig. (**6**) shows the spatial distribution characteristics of the three hydrocarbon components under different particle radii at a migration time of 1.5 s. A larger particle radius leads to narrower pore spaces and smaller throat widths formed by particle packing, making the overall pore structure tighter and the available flow space significantly reduced. Conversely, a smaller particle radius corresponds to a more open pore-throat system. In terms of the overall distribution law, as the particle radius increases from 12.5 mm to 22.5 mm, the pore-throat size decreases continuously. The displacement front propagation distances of all three hydrocarbon components gradually shorten, and the overall swept range shows an obvious shrinking trend. The throttling and retardation effects of the pore structure continue to strengthen.

Different hydrocarbon components show significantly different responses to changes in particle radius, with sensitivity increasing in the order of light component, medium component, and heavy component. The light component is least affected by changes in pore scale. Even in tight pore environments corresponding to large particle radii, it can still invade part of the tiny pore spaces via strong molecular diffusion capacity, maintaining a certain swept range and front propagation ability. The inhibition effect of pore structure restriction on its

migration is limited. The migration behavior of the medium component has moderate sensitivity to particle radius changes. With decreasing pore-throat size, its flow bypassing and local retention phenomena gradually intensify, and the attenuation amplitude of front propagation rate is larger than that of the light component. The constraint effect of the pore structure begins to dominate its migration process. The heavy component is most sensitive to changes in particle radius, and its migration capacity is most strongly controlled by pore scale. With increasing particle radius and narrowing throat width, throat snapping and the Jamin effect are significantly enhanced. Heavy components can barely pass through narrow throats and expand to the upper part of the model, and can only accumulate in the limited large pore space near the injection end. Its distribution range shrinks greatly, the accumulation characteristic is more prominent, and its migration efficiency drops sharply with pore tightening.

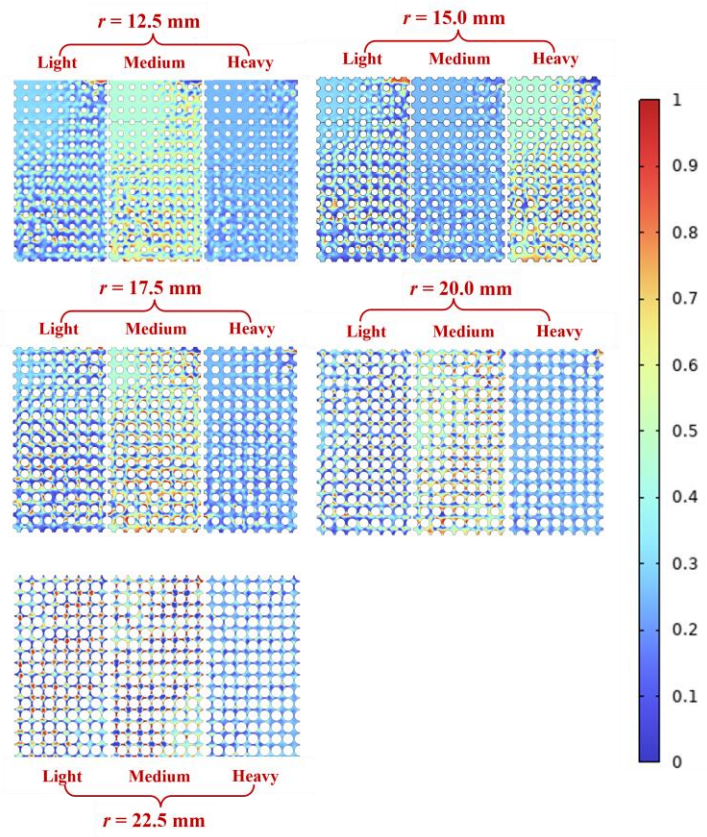

Figure 6: Comparison of distribution characteristics of different hydrocarbon components under various particle radius (1.5 s).

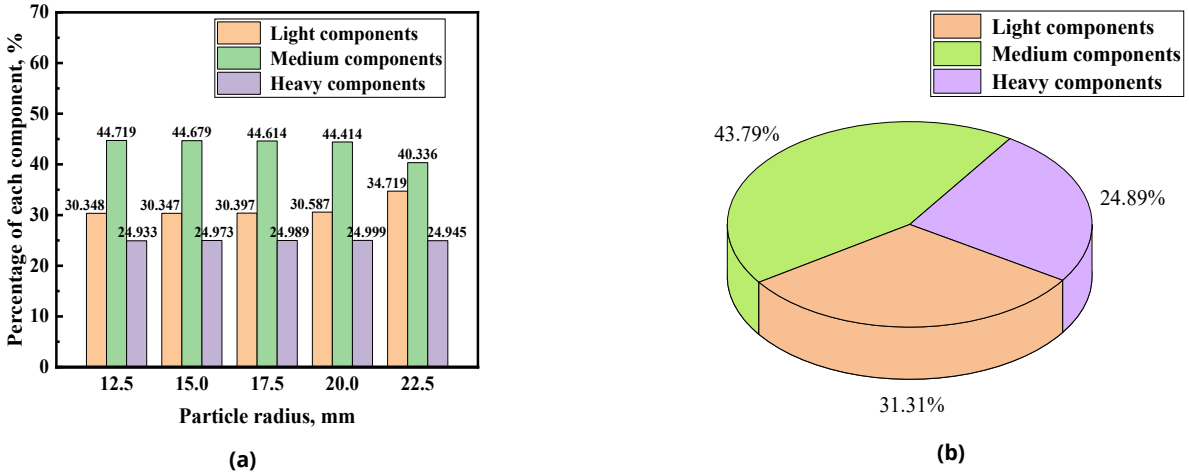

Figure 7: Comparison of distribution area proportions of different hydrocarbon components under various particle radius (1.5 s): **(a)** overall characteristics; **(b)** average values.

Fig. (**7**) compares the distribution area proportions of the three hydrocarbon components under different particle radii at 1.5 s of migration, which quantitatively characterizes the influence of pore structure scale on the degree of component differentiation.

With increasing particle radius and tightening pore throats, the proportion of light components increases gradually, that of medium components shows a decreasing trend, and that of heavy components is generally stable, with only a slight decrease under the maximum particle size. Among them, the proportion of light components has the smallest fluctuation amplitude, reflecting that its molecular diffusion capacity can effectively offset the retardation effect of pore narrowing, and it has stronger pore adaptability. The proportion of medium components decreases steadily with pore tightening, and increased seepage resistance is the dominant factor limiting its migration. The proportion of heavy components changes slightly under most particle sizes. Only when the pore throat shrinks to a critical scale do the restriction effects of throat snapping and the Jamin effect become prominent, leading to a slight decrease in its proportion. The average proportions of the three components over the entire particle size range are 31.31% for light components, 43.79% for medium components, and 24.89% for heavy components, which are mutually verified with the microscopic distribution characteristics.

To quantitatively identify the differentiation threshold, a late-stage decay index of the medium component is defined as $\Gamma_B(r) = [P_B(1.0\ s)\text{-}P_B(1.5\ s)]/P_B(1.0\ s)\times100\%$, where P_B is the distribution area proportion of the medium component. For $r \le 20.0$ mm ($\delta \ge 10$ mm, $\alpha \ge 0.20$), Γ_B remains below 2%, indicating that the medium component proportion is essentially stable throughout the migration process. At $r = 22.5$ mm ($\delta = 5$ mm, $\alpha = 0.10$), Γ_B rises sharply to over 5%, accompanied by a pronounced late-stage decline in the medium component proportion. Adopting $\Gamma_B = 5\%$ as the threshold criterion, the critical particle radius and critical pore-throat width are bracketed as $r_{cr} \in (20.0, 22.5)$ mm and $\delta_{cr} \in (5, 10)$ mm, corresponding to a critical constriction ratio $\alpha_{cr} \in (0.10, 0.20)$. Below this critical throat width, the Jamin effect and throat-snapping become the dominant mechanisms controlling medium-component retention, and the inter-component migration capacity gap is rapidly amplified.

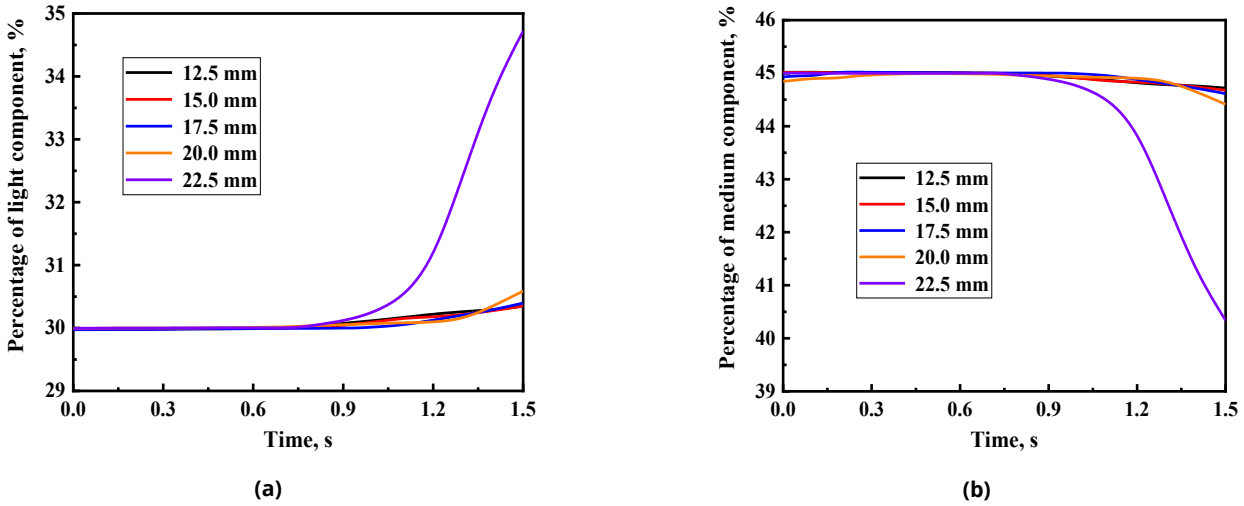

Figure 8: Temporal evolution of distribution area proportions for different hydrocarbon components under various particle radius: **(a)** light components; **(b)** medium components.

Fig. (**8**) further shows the dynamic evolution of the distribution proportions of light and medium components over time. For the light component (Fig. **8a**), its proportion increases continuously with time under all particle size conditions. The growth rate is gentle at small particle sizes, while in the tight environment corresponding to the large particle size of 22.5 mm, its proportion rises rapidly in the late migration stage (>1.0 s). This reflects the continuous driving effect of the diffusion mechanism on light component migration in tight pores. For the medium component (Fig. **8b**), its proportion remains basically stable over time when the particle radius is $r \le 20.0$ mm ($\delta \ge 10$ mm, $\alpha \ge 0.20$). Only under the strong pore constraint of $r = 22.5$ mm ($\delta = 5$ mm, $\alpha = 0.10$) does its proportion decrease significantly in the late migration stage ($t > 1.0$ s), with a relative decay exceeding 5%. This indicates that when the throat width narrows below the critical value $\delta_{cr} \in (5, 10)$ mm, the seepage channels of medium

components are greatly compressed, and their distribution space is continuously occupied by light components with stronger migration capacity.

The threshold provides a direct pore-scale criterion for producibility grading. Zones with dominant throat widths above δ_{cr} ($\alpha > \alpha_{cr}$) allow medium and heavy components to migrate through the throat network, yielding higher oil mobility and more sustainable production; these zones correspond to productive sweet spots. In contrast, zones dominated by sub-critical throats ($\alpha < \alpha_{cr}$) produce mainly light components, while medium and heavy fractions remain trapped by capillary forces, resulting in rapid decline and low ultimate recovery. Practically, the fraction of above-throat pore volume can be quantified from mercury injection capillary pressure (MICP) or nuclear magnetic resonance spectroscopy (NMR) data and mapped across a reservoir interval to identify high-producibility zones. For sub-critical zones, enhanced oil recovery (EOR) methods that reduce interfacial tension (e.g., CO_2 huff-and-puff) are required to mobilize the trapped medium–heavy fractions.

5. Conclusion

This study reveals the multi-component differential migration mechanism of continental shale oil at the pore scale and quantifies how component properties, injection flow rate, and pore structure regulate migration behavior. The main conclusions are as follows:

1. Component properties dominate differential migration and competitive seepage. Light components, with low viscosity and small molecular size, flow and spread most easily, reaching the widest area and continuously expanding their distribution. In contrast, medium and heavy components migrate more slowly because they tend to stick to pore walls (adsorption) and become trapped when their droplets cannot squeeze through narrow throats (the Jamin effect). As light components take over the main flow paths, the space available for medium and heavy components gradually shrinks.
2. Within the range of 1.0 – 3.0 g/s, injection flow rate has only a weak effect on the multi-component distribution pattern. Increasing the flow rate provides a stronger overall driving force but does not change the relative migration ability of the three components. The spatial pattern and proportion of each component remain stable, controlled primarily by component properties and pore structure rather than by injection rate.
3. Pore scale exerts selective regulation on migration with a distinct threshold effect. Heavier components are more sensitive to pore tightening. When the throat width shrinks below the critical value $\delta_{cr} \in (5, 10)$ mm ($r_{cr} \in (20.0, 22.5)$ mm, $\alpha_{cr} \in (0.10, 0.20)$), the inter-component capacity gap widens sharply, with accelerated rise of light component proportion and notable drop of medium component proportion in the late stage. This threshold offers a quantitative pore-scale criterion for sweet spot identification: reservoir intervals with a high proportion of above-critical throats (identified via MICP or NMR) exhibit higher producibility.
4. The model is geometrically upscaled and two-dimensional; although the dimensionless constriction ratio offers a scale-transferable criterion, the absolute nanoscale threshold and three-dimensional connectivity effects require further constraint via pore-network or direct numerical simulation that resolves boundary layers and adsorption films. Interfacial tension and wettability are held constant, whereas in-situ wettability alteration and asphaltene precipitation may shift the threshold in real reservoirs. Direct validation against core flooding or field production data is not yet included; field-scale simulation integrating production profiles is underway and will be reported in future work.

Conflict of interest

The authors declare no conflict of interest.

Funding

Supported by the National Natural Science Foundation of China (No. 52504006), the Collaborative Innovation Project of Colleges in Jinan (No. 202534037), Science-Education-Industry Integration Innovation Special Project of

Qilu University of Technology (No. 2025ZDZX16) and Engineering Research Center of Geothermal Resources Development Technology and Equipment, Ministry of Education, Jilin University.

Data Availability and Materials

The data supporting the findings of this study are available from the corresponding author upon reasonable request.

References

[1] Zhao WZ, Hu SY, Hou LH, Yang T, Li X, Guo BC, *et al*. Types and resource potential of continental shale oil in China and its boundary with tight oil. Pet Explor Dev. 2020; 47(1): 1-11. https://doi.org/10.1016/S1876-3804(20)60001-5

[2] Hu SY, Bai B, Tao SZ, Bian CS, Zhang TS, Chen YY, *et al*. Heterogeneous geological conditions and differential enrichment of medium and high maturity continental shale oil in China. Pet Explor Dev. 2022; 49(2): 257-271. https://doi.org/10.1016/S1876-3804(22)60022-3

[3] Li H, Xu ZQ, Gao XD, Xie JT, Qin QR, Wang HJ, *et al*. Pore structure evolution and geological controls in lacustrine shale systems with implications for marine shale reservoir characterization. Sci Rep. 2025; 15: 17702. https://doi.org/10.1038/s41598-025-02415-y

[4] Zhao W, Jia CZ, Song Y, Li XF, Hou LH, Jiang L, *et al*. Hydrocarbon migration and accumulation simulation: A review and a novel multi-scale quantitative numerical simulation method. Adv Colloid Interface Sci. 2025; 342: 103523. https://doi.org/10.1016/j.cis.2025.103523

[5] Xu F, Li Y, Xu X, Yang J, Xiao F, Shi Y. Thermal-hydrological-mechanical coupling simulation of matrix-type shale oil: Analysis of oil-gas-water multiphase flow mechanism under various parameter conditions. Geoenergy Sci Eng. 2025; 246: 213656. https://doi.org/10.1016/j.geoen.2025.213656

[6] Wang YM, Wang ZL, Zhang ZC, Yao SS, Zhang H, Zheng GQ, *et al*. Recent techniques on analyses and characterizations of shale gas and oil reservoir. Energy Rev. 2024; 3(2): 100067. https://doi.org/10.1016/j.enrev.2023.100067

[7] Will J, Eckardt S. Optimization of Hydrocarbon Production from Unconventional Shale Reservoirs using Numerical Modelling. Int J Pet Technol. 2017; 4: 14-23. https://doi.org/10.15377/2409-787X.2017.04.01.3

[8] Yu CL, Zhang SM, Chen T, Sun ZG, Xu JX. Seepage mode in lamina-developed shale oil reservoirs under strong heterogeneous and strong fluid-solid coupling in Jiyang depression of China. Sci Rep. 2025; 15: 936. https://doi.org/10.1038/s41598-024-84882-3

[9] Li JH, Li YJ, Sang Q, Gong HJ, Xu L, Zhang HY, *et al*. Quantification of seepage characteristics in shale oil reservoirs: A triple medium model-driven approach. Geoenergy Sci Eng. 2024; 242: 213225. https://doi.org/10.1016/j.geoen.2024.213225

[10] Xu S, Wen J, Gou QY, Li QQ, Liu BC. Research Progress and Significance of Shale Oil Micro-Migration. J Earth Sci. 2024; 35: 1765-9. https://doi.org/10.1007/s12583-024-0071-7

[11] Alpak FO, Riviere B, Frank F. A phase-field method for the direct simulation of two-phase flows in pore-scale media using a non-equilibrium wetting boundary condition. Comput Geosci. 2016; 20: 881-908. https://doi.org/10.1007/s10596-015-9551-2

[12] Cai JC, Qin XJ, Xia XZ, Jiao XH, Chen H, Wang H, *et al*. Numerical modeling of multiphase flow in porous media considering micro- and nanoscale effects: A comprehensive review. Gas Sci Eng. 2024; 131: 205441. https://doi.org/10.1016/j.jgsce.2024.205441

[13] Ramstad T, Berg CF, Thompson K. Pore-Scale Simulations of Single- and Two-Phase Flow in Porous Media: Approaches and Applications. Transp Porous Med. 2019; 130: 77-104. https://doi.org/10.1007/s11242-019-01289-9

[14] Li YH, Xu FQ, Xu XY, Bi CQ, Shi Y, Han RB. Investigation on differentiation behaviors of multiple hydrocarbon components in intra-source migration within matrix-type shale oil reservoirs. Fuel 2027; 429(Pt E): 141063. https://doi.org/10.1016/j.fuel.2026.141063

[15] Guan Z, Meng Q, Huang Q, Tang X, Shan Y, Liu G, *et al*. Hydrocarbon micro-migration and differential enrichment mechanism of shale oil in upper Cretaceous Qingshankou Formation in Songliao Basin. Geol J. 2024; 59(5): 1503-19. https://doi.org/10.1002/gj.4952

[16] Anonymous. Molecular dynamics study of shale oil adsorption and diffusion behavior in reservoir nanopores: Impact of hydrocarbon composition and surface type. J Mol Liq. 2024; 414: 126110. https://doi.org/10.1016/j.molliq.2024.126110

[17] Xue CL, Ji DL, Cheng D, Wen YT, Luo HH, Li Y. Adsorption behaviors of different components of shale oil in quartz slits studied by molecular simulation. ACS Omega. 2022; 7(45): 41189-200. https://doi.org/10.1021/acsomega.2c04845

[18] Xiao L, Ju YW, Jin J, Liu J, Tan JQ, Jiang S, *et al*. Micro-nanoscale pore structure characteristics and enrichment mechanisms of shale oil in mixed sedimentary reservoirs of the Jimusar Sag, Junggar Basin, northwestern China. Pet Sci. 2026; 23(3): 1089-104. https://doi.org/10.1016/j.petsci.2025.10.014

[19] Xia DB, Yang ZM, Gao TN, Li HB, Lin W. Characteristics of micro- and nano-pores in shale oil reservoirs. J Pet Explor Prod Technol. 2021; 11: 157-69. https://doi.org/10.1007/s13202-020-01012-1

[20] Li C, Liu XP, Meng LJ, Wang JW, Gao YL, Sun B, *et al*. Fractal heterogeneity characteristics and influenced factors of lacustrine shale pore structure based on N_2 adsorption and mercury injection in the Paleogene Shahejie Formation, Bohai Bay Basin, China. Pet Res. 2026; 9(1): 1-12. https://doi.org/10.1016/j.ptlrs.2026.01.019

[21] Chen ZM, Zhou B, Olorode O, Yu W, Sepehrnoori K. Evaluation of CO_2 sequestration potential in shale reservoirs using an improved embedded discrete fracture model. Int J Rock Mech Min Sci. 2026; 204: 106583. https://doi.org/10.1016/j.ijrmms.2026.106583

[22] Yan GG, Yan WD, Yuan YZ, Gong XJ, Tang ZQ, Bai XY. Research on the method of evaluating the pore throat structure of rock microscopically based on the 3d pore network model of digital core. Int J Pet Technol. 2022; 44: 44-53. https://doi.org/10.54653/2409-787X.2022.09.6

[23] Qu YQ, Ouyang SQ, Gao JW, Shi J, Wu YY, Cheng YT, *et al*. Pore Space Characteristics and Migration Changes in Hydrocarbons in Shale Reservoir. Fractal Fract. 2024; 8(10): 588. https://doi.org/10.3390/fractalfract8100588

[24] Wang WD, Zhang Q, Xu JL, Zheng D, Liu LF, Su YL. Hydrodynamic resistance of pore-throat structures and its effect on shale oil apparent permeability. Int J Coal Sci Technol. 2024; 11: 22. https://doi.org/10.1007/s40789-024-00671-3

[25] Li JL, Ji LL, Jiang WB, Lin M, Mao M, Wei XL, *et al*. Investigation of pore structures and flow transport characteristics of continental shale in Dongying Sag. J Pet Explor Prod Technol. 2025; 15: 163. https://doi.org/10.1007/s13202-025-02079-4

[26] Xu FQ, Song XZ, Song GF, Ji JY, Song ZH, Shi Y, *et al*. Numerical studies on heat extraction evaluation and multi-objective optimization of abandoned oil well patterns in intermittent operation mode. Energy 2023; 269: 126777. https://doi.org/10.1016/j.energy.2023.126777

[27] Gao XY, Yang SL, Zhang YQ, He BY, Wang MY, Hu JT, *et al*. Integrated modeling and economic assessment of hydrogen storage with wellbore-reservoir-thermo-hydro-mechanical-diffusion coupling. Energy 2026; 353: 141065. https://doi.org/10.1016/j.energy.2026.141065

[28] Pati S, Borah A, Boruah MP, Randive PR. Critical review on local thermal equilibrium and local thermal non-equilibrium approaches for the analysis of forced convective flow through porous media. Int Commun Heat Mass Transf. 2022; 132: 105889. https://doi.org/10.1016/j.icheatmasstransfer.2022.105889

[29] Hamidi S, Heinze T, Galvan B, Miller S. Critical review of the local thermal equilibrium assumption in heterogeneous porous media: Dependence on permeability and porosity contrasts. Appl Therm Eng. 2019; 147: 962-71. https://doi.org/10.1016/j.applthermaleng.2018.10.130

[30] Xu FQ, Song XZ, Shi Y, Zhou MM, Wang GS. Erosion damage mechanism of fractured rock mass during cyclic compressed air storage and release in depleted sandstone oil-gas fields. Geoenergy Sci Eng. 2026; 260: 214389. https://doi.org/10.1016/j.geoen.2026.214389

[31] Wang YX, Li HY, Wang ZZ, Xu FQ, Wang TR, Wang C, *et al*. Particle tracing-based numerical investigation of thermal-hydraulic coupling mechanisms and particle transport characteristics in multi-branch well underground thermal energy storage (UTES). Int J Therm Sci. 2026; 230: 111175. https://doi.org/10.1016/j.ijthermalsci.2026.111175

[32] Shi Y, Cui QL, Song XZ, Li GS, Wang GS. Performances of a novel compressed CO_2 energy storage and heat storage integration system using multi-stage hydraulic fractures of horizontal well in subsurface reservoirs. Renew Energy 2025; 251: 123396. https://doi.org/10.1016/j.renene.2025.123396

[33] Li S, Wang GS, Zhou MM, Song XZ, Shi Y, Yi JL, *et al*. Thermal performance of an aquifer thermal energy storage system: Insights from novel multilateral wells. Energy 2024; 294: 130915. https://doi.org/10.1016/j.energy.2024.130915

[34] Feng L, Xiao X, Wang E, Lu C, Li C, Li G, *et al*. Oil mobility evaluation and light hydrocarbon restoration in shale reservoirs: a review. Gondwana Res. 2026; 154: 122-54. https://doi.org/10.1016/j.gr.2025.12.010

[35] Bai Y, Zhao J, Wu W. Methods to determine the upper limits of petrophysical properties in tight oil reservoirs: examples from the Ordos and Songliao Basins. J Pet Sci Eng. 2021; 196: 107983. https://doi.org/10.1016/j.petrol.2020.107983

[36] Xiao Y, Zeng Z, Zhang LQ, Wang JZ, Wang YW, Huang CG. A reduction-consistent phase field model for non-isothermal multiphase flows of N immiscible incompressible fluids. Int J Heat Mass Transf. 2024; 228: 125657. https://doi.org/10.1016/j.ijheatmasstransfer.2024.125657

[37] Lee D, Huh JY, Jeong D, Shin J, Yun A, Kim J. Physical, mathematical, and numerical derivations of the Cahn-Hilliard equation. Comput Mater Sci. 2014; 81: 216-25. https://doi.org/10.1016/j.commatsci.2013.08.027

[38] Liu H, Cheng AJ, Wang H, Zhao J. Time-fractional Allen-Cahn and Cahn-Hilliard phase-field models and their numerical investigation. Comput Math Appl. 2018; 76(8): 1876-92. https://doi.org/10.1016/j.camwa.2018.07.036

[39] Boyer F, Lapuerta C, Minjeaud S, Piar B, Quintard M. Cahn-Hilliard/Navier-Stokes model for the simulation of three-phase flows. Transp Porous Med. 2010; 88: 463-83. https://doi.org/10.1007/s11242-009-9408-z

[40] Djoko J, Koko J. Numerical methods for the Stokes and Navier-Stokes equations driven by threshold slip boundary conditions. Comput Methods Appl Mech Eng. 2016; 305: 936-58. https://doi.org/10.1016/j.cma.2016.03.026

[41] Chen Z, Huan G, Ma Y. Computational Methods for Multiphase Flows in Porous Media. Philadelphia: SIAM; 2006. https://doi.org/10.1137/1.9780898718942

[42] Xu F, Song X, Song Z, Wang G, Shi Y. Heat extraction and interlayer interference in heterogeneous multi-layer commingled production oil reservoir. 56th US Rock Mechanics/Geomechanics Symposium. 2022; Santa Fe, New Mexico, USA, June 2022. Paper Number: ARMA-2022-0504. https://doi.org/10.56952/ARMA-2022-0504